Journal of Materials Chemistry A

PAPER

View Article Online
View Journal | View Issue

Cite this: J. Mater. Chem. A, 2017, 5, 9060

Wafer-scale synthesis of ultrathin CoO nanosheets with enhanced electrochemical catalytic properties†

Fei Wang,‡[a] Yanhao Yu,‡[a] Xin Yin,[a] Peng Tian[ab] and Xudong Wang *[a]

Large area synthesis of two dimensional (2D) nanomaterials with a non-layered crystal structure remains a grand challenge. In this article, we report a solution-based bottom-up synthesis of wafer-scale nanometer-thick CoO nanosheets using ionic layer epitaxy (ILE). In ILE, a monolayer of ionized oleyl sulfate surfactants at the water–air interface served as a flexible template for direct CoO crystallization underneath. The as-synthesized CoO nanosheet is polycrystalline and could be grown as large as the entire solution surface in the reactor (>cm^2) with a uniform 2.8 nm thickness across the entire sheet. The nanosheet is free-standing on the water surface and can be readily transported to arbitrary substrate surfaces for device fabrication. As a demonstration, centimeter-sized CoO nanosheets were directly transferred to Si wafers for electrochemical electrode applications. The nanometer thick CoO nanosheet exhibited higher catalytic properties towards the oxygen evolution reaction (OER) compared to bulk CoO. It also showed excellent stability at high photocurrent density when used as a photoelectrochemical (PEC) photoanode in corrosive alkaline electrolytes. This work evidenced the effectiveness of the ILE technique in synthesizing 2D nanomaterials from a broad range of functional oxides with enhanced physical properties.

Received 1st March 2017
Accepted 10th April 2017

DOI: 10.1039/c7ta01857f

rsc.li/materials-a

Introduction

Discovering and tailoring novel physical properties of materials for application advancements has always been at the center stage of materials science. For a good decade, two dimensional (2D) nanomaterials, referring to those of only one or a few atomic layers thick, have been extensively studied for their exotic physical properties not seen in their bulk form, or any other dimensionalities including one-dimensional (1D) nanowires/nanotubes and zero-dimensional (0D) quantum dots.[1–6] To date, 2D nanomaterials have offered promising opportunities in electronic, optoelectronic, energy, and catalytic applications, thanks to their large surface to volume ratios and distinctive electronic band structures.[7–12] For 2D nanomaterials with naturally layered structures, *e.g.*, graphene and transition metal dichalcogenides (TMDs), a number of strategies have been developed to acquire their 2D form, such as mechanical and liquid phase exfoliation, and chemical vapor deposition. Mechanical exfoliation can produce high quality, single layer 2D materials and is very suitable for studying the fundamental physical properties and developing proof-of-principle devices.[7,13] Liquid phase exfoliation produces large quantities of 2D materials, which enables bulk scale applications such as composite materials.[14,15] Chemical vapor deposition offers a bottom-up approach for depositing a uniform layer of 2D materials which is compatible with thin film technologies and thus promising in future semiconductor industry applications.[16,17] On the other hand, non-layered materials, which offer a far larger variety remain an unexploited territory although unique properties were also discovered in their 2D geometry.[18]

Despite well-documented mechanisms for the synthesis of 1D and 0D nanomaterials,[19,20] little has been known on how to break the symmetry of non-layered crystal structures to create 2D materials with a thickness of few nanometers.[21] In the literature, only a limited number of 2D materials from non-layered crystal structures have been reported, such as PbS, CeO_2, Au, Pd, and Pt nanosheets.[22–25] These nanosheets are generally smaller than 1 μm in their lateral dimension, which remains a grand challenge for device development where access to individual nanosheets is required. Meanwhile, there doesn't appear to be any fundamentally common feature in their formation mechanisms. Therefore, an even bigger challenge lies in preparing 2D materials beyond naturally-layered materials with appreciable size, and novel synthesis mechanisms are required for this task.

To address this task, we previously reported few nanometers thick, single crystalline ZnO nanosheets by ionic layer epitaxy (ILE).[26] In ILE, an ionic amphiphilic molecular monolayer at

[a]Materials Science and Engineering, University of Wisconsin-Madison, Madison, Wisconsin 53706, USA. E-mail: xudong.wang@wisc.edu

[b]School of Chemical Engineering, Dalian University of Technology, Dalian, 116024, P. R. China

† Electronic supplementary information (ESI) available. See DOI: 10.1039/c7ta01857f

‡ These authors contributed equally to this work.

a two-phase interface, typically a water–air interface, is employed and crystals grow at the interface directed by electrostatic and covalent interactions between the precursor ions and the functional groups on the amphiphilic molecules. Fundamentally, this strategy has no restriction on the intrinsic crystal structure of targeting materials, and thus provides an unprecedented platform for universally manufacturing non-layered materials, such as metal oxides. Take a specific example, cobalt oxides and hydroxides are promising oxygen evolution catalysts (OER) due to appropriate binding energy between Co atom and OER species.[27–31] 2D cobalt materials have shown promoted catalytic performance over their bulk counterpart.[32] Current strategies to obtain 2D cobalt-based catalysts include hydrothermal reaction, electrodeposition and atomic layer deposition. They require harsh preparation conditions, conductive substrates, or sophisticated equipment.[33–35] Producing wafer scale, continuous, and nanometer-thick cobalt oxide thin sheets is so far impractical. In this work, we report the ILE growth of large area, ultrathin CoO nanosheets grown at the water–air interface directed by oleic acid monolayers. The CoO nanosheets could be as large as the opening area of the reactor and thus enabled large-scale applications of its 2D morphology. We examined the electrochemical properties of these CoO nanosheets and discovered significant performance gain for photoelectrochemical (PEC) water splitting in comparison to their bulk form.

Results and discussions

Fig. 1 schematically illustrates the synthesis and transfer of CoO nanosheets. The aqueous nutrient solution contains cobalt(II) nitrate hexahydrate and hexamethylenetetramine (HMT). The solution surface was covered with a monolayer of ionized oleyl sulfate surfactants. As revealed in our previous work, the presence of the ionic oleic acid monolayer is critical for the formation of ultrathin nanosheets with macroscopic continuity. It has been well documented in the literature that ionic and covalent interactions exist between Langmuir monolayers and metal ions in the aqueous phase, and the interactions are particularly stronger for multivalent metal ions.[36] Due to the weak alkaline pH environment buffered by HMT, the protons on carboxylic groups were mostly dissociated, and therefore the monolayer had a negative local electrical field. This hypothesis can be validated by the pH-pK_a relationship. At 60 °C, 25 mM HMT decomposed to HCHO and ammonium hydroxide, yielding a pH value of 11.125. The pK_a of oleic acid is 9.85.[37] When the pH is equal to pK_a, 50% of the acid will be dissociated. At pH of 11.125, over 90% of oleic acid will be dissociated as presumed. As a result of the negative local charges, cobalt ions were concentrated underneath the monolayer, and a continuous stern layer of cobalt ions formed underneath the monolayer (Fig. 1a). In this alkaline environment, cobalt ions in the stern layer could reach supersaturation and crystallize into a layer of nanocrystals. With the carboxylic head groups bonding to CoO crystals and thus reduced surface energy, the critical nucleation size of CoO was reduced as well.[38] These nanocrystals then merged together into a continuous macroscopic sheet without further increasing the thickness (Fig. 1b). The final nanosheet

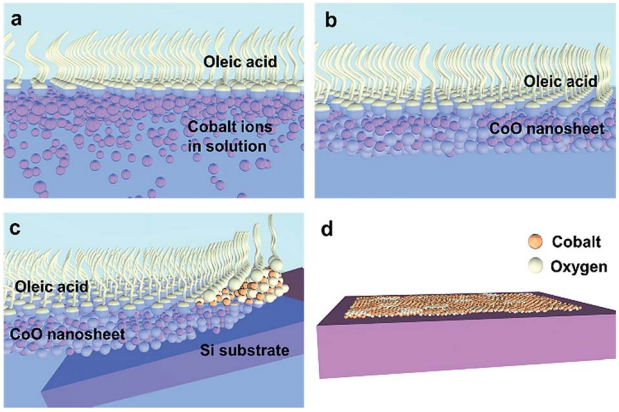

Fig. 1 Schematic illustration of the formation and processing of CoO nanosheets. (a) At the water–air interface, amphiphilic molecules (oleic acid) form a close-packed monolayer under which aqueous Co ions are concentrated and form a stern layer. (b) Co ions crystalize into macroscopic, continuous nanocrystalline CoO nanosheets as large as the water–air interface. (c) An arbitrary substrate can be dipped into the aqueous phase and the free-standing CoO nanosheet was lifted up. (d) The surfactant layer can be removed by post-treatment after the nanosheet was transferred to a substrate.

products were continuous and covered the entire solution surfaces. To transfer the nanosheet, a Si substrate was dipped into the solution from the side of the reactor at an angle and then lifted up (Fig. 1c). The surface organic surfactant layer could be further removed by plasma treatment, leaving a flat and ultrathin CoO nanosheet on the entire Si substrate surface (Fig. 1d).

Fig. 2a is a low magnification SEM image showing an as-transferred CoO nanosheet on a Si substrate over a very large area. No obvious contrast variation could be observed because the nanosheet was continuous and uniform in thickness. There were no wrinkles or overlaps of the as-transferred nanosheet either. Sporadic brighter dots could be found on the nanosheets (which could be more clearly observed from the high-magnification SEM image in Fig. S1a†). They are nanoparticles picked up from the reaction solution during the transfer process. Formation of these nanoparticles is a homogeneous nucleation that competes with ILE at the interface. Some cracks (the slight brighter regions in the SEM image, Fig. 2a and S1b†) were also observed on the nanosheets, which were likely formed during the transfer and drying. These occasional cracks offered a good observation area to determine the nanosheet thickness. One representative small crack area was selected as highlighted by a dashed box in Fig. S1b,† and the topography was scanned by using atomic force microscopy (AFM). As shown in Fig. 2b, the nanosheet surface was fair smooth and flat with an average roughness factor (R_a) of only 0.39 nm, which was comparable to the reported amorphous metal oxide film.[39] A line profile along the crack area was extracted and shown in Fig. 2c, which revealed the thickness of the nanosheets was 2.8 nm. The small cracked chips inside the gap also had the same 2.8 nm thickness, further suggesting that the small pieces might come off from the nanosheet post growth, *i.e.* during transferring.

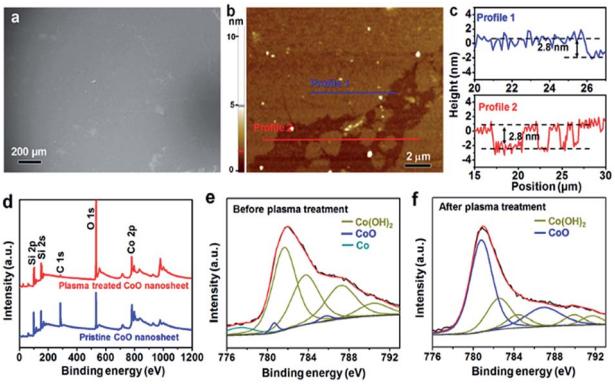

Fig. 2 Characterization of CoO nanosheets. (a) SEM image of a CoO nanosheet covering a Si substrate surface. (b) AFM topography scan of a cracking area from the CoO nanosheet on a Si wafer. (c) The height profile along the blue and red lines in (b) showing a very small roughness factor of 0.39 nm and a uniform film thickness of 2.8 nm. (d) XPS spectra of CoO nanosheets before (blue) and after (red) oxygen plasma treatment. (e) and (f) XPS of CoO nanosheets before and after O_2 plasma treatment.

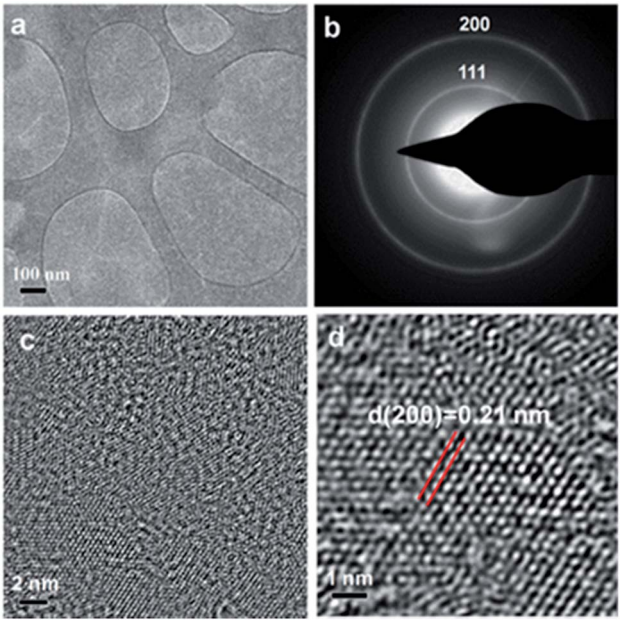

Fig. 3 TEM characterization of CoO nanosheets. (a) A low magnification image of a CoO nanosheet supported by a holey carbon TEM grid. (b) Electron-diffraction pattern of CoO nanosheets shown in (a). (c) HRTEM image of the CoO nanosheet showing its polycrystalline nature with an average grain size ~3 nm. (d) HRTEM image showing the lattice of CoO grains and grain boundaries revealing the fully crystallized nanosheets structure.

The crystal structure of the nanosheet was identified by grazing-angle X-ray diffraction (GAXRD). Fig. S2† shows the (111) and (200) peaks of CoO (JCPDS no. 001-1227), indicating a polycrystalline CoO structure with no preferred orientation. The diffraction pattern was acquired up to a 2θ angle of 45° due to the instrument limitation on the angle of 2D detector when the incident angle was close to zero. X-ray photoelectron spectroscopy (XPS) was employed to probe the elemental features and bonding states of this CoO nanosheet. The full XPS survey spectra clearly showed the Co, O and C peaks detected from the as-transferred pristine CoO nanosheets on a Si substrate (blue curve in Fig. 2d). The C signal originated from the oleyl acid surfactant coverage. The surfactant residues could be removed by using oxygen plasma. The largely reduced C signal in plasma-treated samples confirmed the successful removal of C residue after 10 minutes of oxygen plasma treatment (red curve in Fig. 2d). To further reveal the chemical environment of the Co atom, the Co 2p peak of both pristine and plasma-treated CoO nanosheets was individually scanned and deconvoluted. In pristine CoO nanosheets, the majority of surface Co atoms were bonded with the OH^- group due to surfactant binding (Fig. 2e). After plasma treatment, the majority peak intensity of the Co 2p spectrum could be attributed to the Co–O bonds (Fig. 2f), evidencing that the bulk component of this nanosheet was CoO. This was consistent with XRD observations.

Transmission electron microscopy (TEM) was used to further characterize the crystal structure of CoO nanosheets. Fig. 3a shows the as-synthesized nanosheet at a low magnification on a holey carbon TEM grid. Due to the complete coverage and uniform thickness of the nanosheet, no distinct morphological features can be observed at low magnification. The ring-pattern of electron diffraction (Fig. 3b) revealed the polycrystalline nature of the nanosheets, where continuous diffraction rings of the (111) and (200) facets can be indexed agreeing well with the XRD spectra. The polycrystalline feature was clearly revealed by the high-resolution TEM (HRTEM) image shown in Fig. 3c. The average grain size was ~3 nm, which approximated to the thickness of the nanosheet. This feature suggested that the nanosheets were formed *via* in-plane merging of anisotropic CoO nanocrystals that were nucleated underneath the surfactant monolayer, as we proposed in our previous work.[26] Fig. 3d shows a HRTEM image of a single CoO grain (Fig. 3d) with its (111) surface oriented in parallel with the incident beam. From the image, the (200) *d*-spacing was measured to be 0.21 nm. No amorphous region was found along the grain boundaries, confirming that the entire film is completely crystallized.

This ultrathin nanosheet possessed two advantages for catalyst applications: abundant surface active sites for binding chemicals, and the short charge diffusion length along the out-of-plane direction. To study its catalytic properties associated with its ultra-small thickness towards the OER, the CoO nanosheet was transferred onto a heavily doped p-type Si (denoted as p^+-Si) substrate. As a comparison, the OER activity of CoO bulk materials was evaluated using the same p^+-Si substrate. The bulk CoO film (~1 μm in thickness) was deposited on the silicon wafer using a modified thermal annealing procedure (Fig. S3,† see the Experimental section for details).[40] XRD spectra of the bulk CoO displayed identical (111) and (200) peak positions as the CoO nanosheets (Fig. S4†), confirming that both the bulk film and nanosheet had the same phase. Fig. 4a illustrates the current density–potential (*J*–*V*) curves of CoO nanosheets (blue) and bulk CoO (red) measured in 1 M NaOH aqueous solution. The *J*–*V* curves were collected at a steady state (Fig. S5†). Bulk CoO could only produce a geometric current density of 0.8 mA

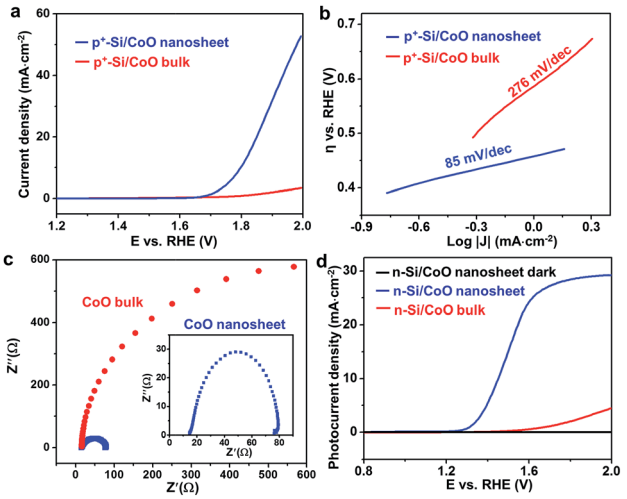

Fig. 4 Electrocatalytic performance of CoO nanosheets and bulk CoO films for the OER. (a, b) Current density–potential (J–V) curves (a) and Tafel slopes (b) of CoO nanosheets and bulk CoO films measured in 1 M NaOH aqueous solution. (c) Nyquist plots recorded at 1.9 V *vs.* the RHE in 1 M NaOH aqueous solution. The inset is the amplified plot of CoO nanosheets. (d) Photocurrent density–potential (J_{ph}–V) curves of the n-Si/CoO nanosheet and n-Si/CoO bulk film measured in 1 M NaOH aqueous solution under 1 Sun illumination.

cm^{-2} at an overpotential (η) of 560 mV (*vs.* the reversible reference electrode (RHE)). At the same η of 560 mV *vs.* the RHE, the CoO nanosheet was able to achieve a geometric current density of 10 mA cm^{-2}, which was 12.5 times larger than that of the CoO bulk.

By extrapolating the linear region of η *versus* log J (Fig. 4b), the Tafel slope of the bulk CoO was determined to be 276 mV per decade, suggesting the slow charge transfer kinetics between bulk CoO and the electrolyte. Nevertheless, when the film thickness shrunk down to 2 nm, the Tafel slope was sharply reduced to 85 mV per decade, indicating a largely promoted interfacial kinetic compared to its bulk form. Table 1 compares the OER performance of the ultrathin CoO nanosheets with other reported CoO geometries. In general, the Tafel slope of the ultrathin CoO nanosheet was fairly low and only one quarter of the reported pristine CoO nanoparticles.[41] Compared to the benchmark defective ALD CoO_x, the CoO nanosheet could still deliver a comparable η at a current density of 10 mA cm^{-2}.[34]

Similar surface kinetic variation was also revealed by the Nyquist plots obtained from electrochemical impedance spectroscopy. The recorded semicircle manifests the charge transfer resistance between the catalysis and the electrolyte interface. As shown in Fig. 4c, the semicircle radius of CoO nanosheets was at least 10 times smaller than that of bulk CoO, suggesting a substantial reduction of charge transfer resistance of/across the solid/electrolyte interface. Such a significant improvement was a direct result of the nanometer film thickness as well as the largely increased surface Co atom ratio. The ultra-small film thickness ensured an efficient hole transportation with only a couple of nanometers charge diffusion length. It is also known that low-coordinated surface transitional metal cations could serve as predominate adsorption sites for electrochemical reactants (*e.g.*, CO_2 and H_2O).[42,43] Therefore, rapid charge transport kinetics and very high OER rates were achieved by the nanometer-thick CoO nanosheet.

Table 1 OER performance comparison for the CoO nanosheet and other CoO geometries

CoO based OER catalyst	Tafel slope (mV dec^{-1})	η (mV *vs.* the RHE) at J = 10 mA cm^{-2}
CoO nanosheet	85	560
CoO bulk	276	870
ALD grown CoO_x (ref. 34)	50–70	470–670
CoO nanoparticle (NP)[41]	354	510

The ILE-grown CoO nanosheet also offered a wafer-scale film size and continuous film structure, which greatly favored direct integration of the nanosheets with light absorbers, providing an unprecedented platform for developing binder-free photoelectrochemical (PEC) devices. These merits distinguished ILE nanosheets from other 2D nanomaterial systems that were typically micro- or nanometers in size and required additional polymer binders for large-scale catalyst manufacturing. To demonstrate this advantage, we fabricated a PEC cell by simply laying the CoO nanosheet on the surface of a n-Si wafer and measured the PEC performance with ~0.1 cm^2 active area in 1 M NaOH aqueous solution under one sun illumination (AM 1.5G). As shown in Fig. 4d, the onset potential of the n-Si/CoO nanosheet was located at the position of ~1.29 V *vs.* the RHE, comparable to other Si photoanodes without a buried junction.[44] The saturated photocurrent density (J_{ph}) reached 28.1 mA cm^{-2} at 1.76 V *vs.* the RHE, on par with that of typical planar Si photoelectrodes.[45] The fairly low onset potential and high J_{ph} evidenced effective coupling between the photoactive n-Si and electrochemically active CoO nanosheet under no binder conditions. On the other hand, the n-Si/bulk CoO exhibited very limited PEC performance, probably caused by the low catalytic ability and profound light blocking by the thick CoO film. By comparing the J–V curves of the n-Si/CoO nanosheet and p^+-Si/CoO nanosheet, the photovoltage generated by the light absorbing n-Si was estimated to be 0.34 V (Fig. S6†).

To further maximize the operational stability of Si/CoO nanosheet photoelectrodes, a uniform TiO_2 layer grown by atomic layer deposition (ALD) was introduced to isolate the Si surface from the corrosive NaOH aqueous solution, as schematically shown in the inset of Fig. 5a. The amorphous ALD TiO_2 has shown great promise in universally protecting Si and III–IV group of composite photoelectrodes without compromising any photoconversion efficiency.[46,47] Fig. 5a compares the J–V curves of the p^+-Si/CoO nanosheet system with and without TiO_2 protection. In this case, slight reduction of J was observed after adding the TiO_2 layer, probably caused by a modest current loss in the TiO_2 film. The durability of the n-Si/TiO_2/CoO nanosheet was then assessed in 1 M NaOH aqueous solution by recording the photocurrent density as a function of time (J_{ph}–t) at a constant external bias of 1.48 V *vs.* the RHE. As shown in Fig. 5b, J_{ph} of the n-Si/TiO_2/CoO nanosheet exhibited no

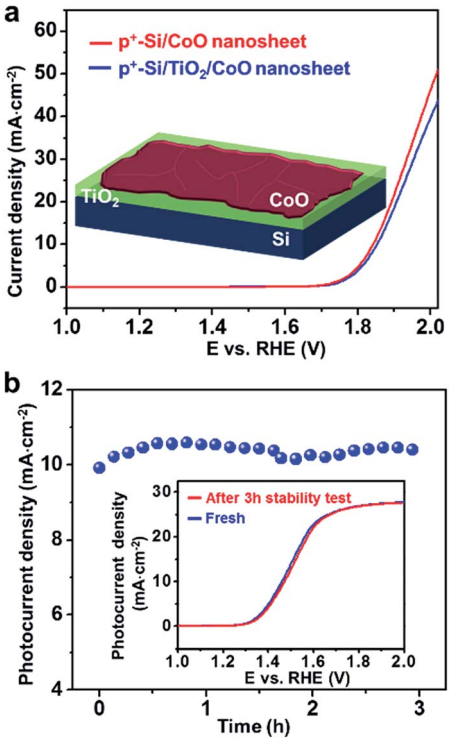

Fig. 5 Photoelectrochemical (PEC) stability evaluation of n-Si/CoO nanosheet photoelectrodes. (a) *J*–*V* curves of the p^+-Si/CoO nanosheet and p^+-Si/TiO_2/CoO nanosheet measured in 1 M NaOH aqueous solution. The inset is the schematic showing the device configuration of the Si/TiO_2/CoO nanosheet photoelectrode. (b) Photocurrent density–time (J_{ph}–*t*) curves of the n-Si/TiO_2/CoO nanosheet recorded with a constant external bias of 1.48 V (*vs.* the RHE). The inset is the J_{ph}–*V* curves of the n-Si/TiO_2/CoO nanosheet before (blue) and after (red) 3 hours of PEC reaction, demonstrating the stability of the CoO nanosheet.

tendency of reduction after 3 hours of continuous PEC reaction. The nearly identical *J*–*V* behaviors of the n-Si/TiO_2/CoO nanosheet before and after 3 hours of operation reinforced the excellent stability of the n-Si/TiO_2/CoO nanosheet electrode (inset of Fig. 5b). The long lifetime confirmed that the ILE-grown CoO nanosheet had strong endurance to the corrosive electrochemical reaction environment. No cracks or any other types of damage were observed from the CoO nanosheet after 3 h of PEC reaction (Fig. S7†). The good electrochemical stability was mainly a result of the short out-plane charge diffusion length enabled by the unique ultrathin 2D structure, which could drastically facilitate the charge transportation and avoid the formation of hot spots, and thus reduce the corrosion rate of the CoO nanosheet.[35] Under the anodic bias, it is also possible to form a thin Co_3O_4 layer (known as a stable OER catalyst) at the interface of TiO_2 and the CoO nanosheet.[48] This may also contribute to the good durability of the PEC device.

Conclusions

In summary, we reported a large-scale nanometer-thick polycrystalline CoO nanosheet fabricated by a facile ILE approach. The film size could reach wafer scale and the film thickness was only 2.8 nm. This CoO nanosheet achieved significantly higher OER catalytic performance compared with bulk CoO owing to the very large surface atom ratio and ultra-small cross-plane charge diffusion length. At a η of 560 mV *vs.* the RHE, the CoO nanosheet delivered a geometric current density of 10 mA cm^{-2}, which was more than one order of magnitude higher than the bulk CoO film (0.8 mA cm^{-2} at the same η). The Tafel slope of the CoO nanosheet was estimated to be 85 mA per decade, which was more than 3 times smaller than that of bulk CoO (276 mA per decade). The wafer-scale film size significantly facilitated the integration of the CoO nanosheet with a light absorbing n-type silicon wafer, enabling an efficient PEC photoanode with an onset potential of ~1.29 V *vs.* the RHE and a J_{ph} of 28.1 mA cm^{-2} at 1.76 V *vs.* the RHE. After coupling with an ALD TiO_2 protection layer, this photoanode was able to continuously work for more than 3 hours in 1 M NaOH aqueous solution without any observable performance decay. This is the first solution-based bottom-up synthesis of nanometer-thick CoO nanosheets, which exhibited drastically enhanced catalytic properties compared to its bulk form. Although rigid Si substrates were used, ILE inherently has the compatibility with flexible devices due to the low-temperature synthesis and facile transfer process. This work shows the promise of the ILE technique in synthesizing 2D nanomaterials from a broad range of functional oxides with unprecedented performance gains.

Experimental section

Synthesis of CoO nanosheets

The aqueous nutrient solution containing 2 mM cobalt(II) nitrate hexahydrate and 2 mM hexamethylenetetramine (HMT) was gently added to a glass reaction vial while minimizing any wetting of the glass wall above the water–air interface. Depending on the opening area of the glass vial, a calculated amount of chloroform solution of oleyl sulfate sodium salt was added to the water–air interface. For a glass vial with 4.5 cm^2 opening area, 8 μL of surfactant solution with a concentration of 2 mg oleyl sulfate sodium salt in 10 mL chloroform were used. After about 5 minutes, the glass vial was capped and placed in a convection oven at 60 °C. The reaction time ranged from 2 hours to 6 hours depending on the target thickness.

Fabrication of electrochemical and photoelectrochemical (PEC) devices

The assembly of the PEC cell started from cleaning Si wafers. A 380 μm-thick, phosphorus doped, single-side polished, ⟨100⟩ oriented, n-type Si wafer with resistivity of 1–10 Ω cm was first cleaned sequentially in the ultrasonic bath of isopropanol and distilled (DI) water. The wafer was then immersed in 5 wt% HF aqueous solution for 30 seconds to remove the native oxide. After that, the wafer was dipped into the reaction container and the CoO nanosheet was lifted up. To eliminate the unwanted surfactant layer and enhance the adhesion between Si and the CoO nanosheet, the Si/CoO nanosheet was exposed to 300 W O_2 plasma for 10 minutes and then annealed at 400 °C in a N_2 atmosphere for 1 hour. Subsequently, the back side of the Si/

CoO nanosheet was scratched with a diamond scribe, and then was coated with a Ga/In eutectic mixture and connected to a metal lead, forming an ohmic back contact. The metal lead was then affixed by the silver paint. After drying, the entire back side and partial front side of Si/CoO nanosheet were encapsulated in epoxy, yielding an exposed active area of ~0.1 cm^2. Calibrated digital image and ImageJ were used to determine the active area established by epoxy. The electrochemical device was built in a similar way except changing the n-Si to a 380 μm-thick, boron heavily doped, single-side polished, ⟨100⟩ oriented, p type wafer with a resistivity of 0.001–0.005 Ω cm. For the CoO bulk sample, 0.5 M Co $(NO_3)_2 \cdot 6H_2O$ ethanol solution was dropped on the Si wafer surface. The wafer was then transferred to a tube furnace and annealed at 1000 °C for 10 hours in an Ar atmosphere. The following device fabrication process was similar to that of the CoO nanosheet.

Electrochemical and PEC measurements

The electrochemical measurements were conducted with a typical three-electrode setup with the n-Si/CoO nanosheet as the working electrode, a Pt wire as the counter electrode and a saturated calomel electrode (SCE) as the reference electrode. All electrodes were immerged in a 1 M NaOH aqueous electrolyte and the working electrode was illuminated by one sun illumination. J_{ph}–V and J_{ph}–t curves were recorded using an Autolab PGSTAT302N station. J_{ph}–t curves were measured at a constant external bias of 1.48 V *vs.* the RHE. SCE was converted to the RHE using the following relationship: $E(\mathrm{RHE}) = E(\mathrm{SCE}) + 0.244\ \mathrm{V} + 0.059 \times \mathrm{pH}$. The electrochemical impedance measurements were conducted by applying a 5 mV bias to the sample and sweeping the frequency from 100 kHz to 100 mHz.

Characterization

SEM measurements were carried out on a Zeiss Leo 1530 field emission microscope and TEM observation were done on a FEI TF30 microscope (300 kV). The accelerating voltage and working distance of SEM were 5 kV and 3 mm, respectively. X-ray diffraction patterns were acquired from the Bruker D8 Discovery with Cu Kα radiation (0.15418 nm) and an entrance slit of 0.5 mm. The grazing-angle X-ray diffraction was recorded using a decoupled theta-two theta mode with an incident angle of 4°. XPS was obtained from a Thermo Scientific K-alpha XPS instrument with a 400 μm spot size. The flood gun of the XPS instrument was turned on during the measurement. For the SEM, XRD and XPS measurements, the CoO nanosheets were transferred to s SiO_2-coated Si wafer (1 cm × 1 cm) by dipping the substrate into the reaction solution from the side of the reactor and then lifting up. After transfer, the substrates with CoO nanosheets were dried naturally in air. TEM samples were collected in a similar way by replacing the Si wafer with a holey carbon TEM grid.

Acknowledgements

This work is supported by Army Research Office (ARO) under grant W911NF-16-1-0198 and the National Science Foundation through the University of Wisconsin Materials Research Science and Engineering Center (DMR-1121288).

References

1 K. S. Novoselov, A. Mishchenko, A. Carvalho and A. H. Castro Neto, *Science*, 2016, **353**, aac9439.
2 L. A. Ponomarenko, R. V. Gorbachev, G. L. Yu, D. C. Elias, R. Jalil, A. A. Patel, A. Mishchenko, A. S. Mayorov, C. R. Woods, J. R. Wallbank, M. Mucha-Kruczynski, B. A. Piot, M. Potemski, I. V. Grigorieva, K. S. Novoselov, F. Guinea, V. I. Fal'ko and A. K. Geim, *Nature*, 2013, **497**, 594–597.
3 H. Zhu, Y. Wang, J. Xiao, M. Liu, S. Xiong, Z. J. Wong, Z. Ye, Y. Ye, X. Yin and X. Zhang, *Nat. Nanotechnol.*, 2015, **10**, 151–155.
4 A. A. Balandin, *Nat. Mater.*, 2011, **10**, 569–581.
5 X. Duan, C. Wang, A. Pan and R. Yu, *Chem. Soc. Rev.*, 2015, **44**, 8859–8876.
6 S. Z. Butler, S. M. Hollen, L. Cao, Y. Cui, J. A. Gupta, H. R. Gutierrez, T. F. Heinz, S. S. Hong, J. Huang, A. F. Ismach, E. Johnston-Halperin, M. Kuno, V. V. Plashnitsa, R. D. Robinson, R. S. Ruoff, S. Salahuddin, J. Shan, L. Shi, M. G. Spencer, M. Terrones, W. Windl and J. E. Goldberger, *ACS Nano*, 2013, **7**, 2898–2926.
7 W. Wu, L. Wang, Y. Li, F. Zhang, L. Lin, S. Niu, D. Chenet, X. Zhang, Y. Hao, T. F. Heinz, J. Hone and Z. L. Wang, *Nature*, 2014, **514**, 470–474.
8 Y. Gong, J. Lin, X. Wang, G. Shi, S. Lei, Z. Lin, X. Zou, G. Ye, R. Vajtai, B. I. Yakobson, H. Terrones, M. Terrones, B. K. Tay, J. Lou, S. T. Pantelides, Z. Liu, W. Zhou and P. M. Ajayan, *Nat. Mater.*, 2014, **13**, 1135–1142.
9 H. Li, C. Tsai, A. L. Koh, L. Cai, A. W. Contryman, A. H. Fragapane, J. Zhao, H. S. Han, H. C. Manoharan, F. Abild-Pedersen, J. K. Norskov and X. Zheng, *Nat. Mater.*, 2016, **15**, 364.
10 M. Liu, X. Yin, E. Ulin-Avila, B. Geng, T. Zentgraf, L. Ju, F. Wang and X. Zhang, *Nature*, 2011, **474**, 64–67.
11 G. Ye, Y. Gong, J. Lin, B. Li, Y. He, S. T. Pantelides, W. Zhou, R. Vajtai and P. M. Ajayan, *Nano Lett.*, 2016, **16**, 1097–1103.
12 M. A. Lukowski, A. S. Daniel, F. Meng, A. Forticaux, L. Li and S. Jin, *J. Am. Chem. Soc.*, 2013, **135**, 10274–10277.
13 H. Li, J. Wu, Z. Yin and H. Zhang, *Acc. Chem. Res.*, 2014, **47**, 1067–1075.
14 J. Zheng, H. Zhang, S. Dong, Y. Liu, C. T. Nai, H. S. Shin, H. Y. Jeong, B. Liu and K. P. Loh, *Nat. Commun.*, 2014, **5**, 2995.
15 D. Hanlon, C. Backes, E. Doherty, C. S. Cucinotta, N. C. Berner, C. Boland, K. Lee, A. Harvey, P. Lynch, Z. Gholamvand, S. Zhang, K. Wang, G. Moynihan, A. Pokle, Q. M. Ramasse, N. McEvoy, W. J. Blau, J. Wang, G. Abellan, F. Hauke, A. Hirsch, S. Sanvito, D. D. O'Regan, G. S. Duesberg, V. Nicolosi and J. N. Coleman, *Nat. Commun.*, 2015, **6**, 8563.
16 W. Strupinski, K. Grodecki, A. Wysmolek, R. Stepniewski, T. Szkopek, P. E. Gaskell, A. Gruneis, D. Haberer, R. Bozek, J. Krupka and J. M. Baranowski, *Nano Lett.*, 2011, **11**, 1786–1791.

17 G. H. Lee, R. C. Cooper, S. J. An, S. Lee, A. van der Zande, N. Petrone, A. G. Hammerberg, C. Lee, B. Crawford, W. Oliver, J. W. Kysar and J. Hone, *Science*, 2013, **340**, 1073–1076.
18 D. Deng, K. S. Novoselov, Q. Fu, N. Zheng, Z. Tian and X. Bao, *Nat. Nanotechnol.*, 2016, **11**, 218–230.
19 R. S. Wagner and W. C. Ellis, *Appl. Phys. Lett.*, 1964, **4**, 89–90.
20 F. Meng, S. A. Morin, A. Forticaux and S. Jin, *Acc. Chem. Res.*, 2013, **46**, 1616–1626.
21 F. Wang and X. Wang, *Nanoscale*, 2014, **6**, 6398–6414.
22 C. C. Li, W. P. Cai, B. Q. Cao, F. Q. Sun, Y. Li, C. X. Kan and L. D. Zhang, *Adv. Funct. Mater.*, 2006, **16**, 83–90.
23 G. B. Bhandari, K. Subedi, Y. He, Z. Jiang, M. Leopold, N. Reilly, H. P. Lu, A. T. Zayak and L. Sun, *Chem. Mater.*, 2014, **26**, 5433–5436.
24 F. Saleem, Z. Zhang, B. Xu, X. Xu, P. He and X. Wang, *J. Am. Chem. Soc.*, 2013, **135**, 18304–18307.
25 X. Huang, S. Tang, X. Mu, Y. Dai, G. Chen, Z. Zhou, F. Ruan, Z. Yang and N. Zheng, *Nat. Nanotechnol.*, 2011, **6**, 28–32.
26 F. Wang, J. H. Seo, G. Luo, M. B. Starr, Z. Li, D. Geng, X. Yin, S. Wang, D. G. Fraser, D. Morgan, Z. Ma and X. Wang, *Nat. Commun.*, 2016, **7**, 10444.
27 J. K. Norskov, T. Bligaard, J. Rossmeisl and C. H. Christensen, *Nat. Chem.*, 2009, **1**, 37–46.
28 M. W. Kanan and D. G. Nocera, *Science*, 2008, **321**, 1072–1075.
29 J. D. Blakemore, H. B. Gray, J. R. Winkler and A. M. Müller, *ACS Catal.*, 2013, **3**, 2497–2500.
30 B. M. Hunter, H. B. Gray and A. M. Müller, *Chem. Rev.*, 2016, **116**, 14120–14136.
31 Y. Yu, Z. Zhang, X. Yin, A. Kvit, Q. Liao, Z. Kang, X. Yan, Y. Zhang and X. Wang, *Nat. Energy*, 2017, **2**, 17045.
32 S. Gao, Y. Lin, X. Jiao, Y. Sun, Q. Luo, W. Zhang, D. Li, J. Yang and Y. Xie, *Nature*, 2016, **529**, 68–71.
33 J. C. Hill, A. T. Landers and J. A. Switzer, *Nat. Mater.*, 2015, **14**, 1150–1155.
34 J. Yang, J. K. Cooper, F. M. Toma, K. A. Walczak, M. Favaro, J. W. Beeman, L. H. Hess, C. Wang, C. Zhu, S. Gul, J. Yano, C. Kisielowski, A. Schwartzberg and I. D. Sharp, *Nat. Mater.*, 2017, **16**, 335–341.
35 S. Gao, X. Jiao, Z. Sun, W. Zhang, Y. Sun, C. Wang, Q. Hu, X. Zu, F. Yang, S. Yang, L. Liang, J. Wu and Y. Xie, *Angew. Chem., Int. Ed. Engl.*, 2016, **55**, 698–702.
36 T. Bala, B. L. Prasad, M. Sastry, M. U. Kahaly and U. V. Waghmare, *J. Phys. Chem. A*, 2007, **111**, 6183–6190.
37 J. R. Kanicky and D. O. Shah, *J. Colloid Interface Sci.*, 2002, **256**, 201–207.
38 M. A. Boles, D. Ling, T. Hyeon and D. V. Talapin, *Nat. Mater.*, 2016, **15**, 364.
39 M. G. Kast, E. A. Cochran, L. J. Enman, G. Mitchson, J. Ditto, C. Siefe, P. N. Plassmeyer, A. L. Greenaway, D. C. Johnson, C. J. Page and S. W. Boettcher, *J. Am. Chem. Soc.*, 2016, **138**, 16800–16808.
40 L. Liao, Q. Zhang, Z. Su, Z. Zhao, Y. Wang, Y. Li, X. Lu, D. Wei, G. Feng, Q. Yu, X. Cai, J. Zhao, Z. Ren, H. Fang, F. Robles-Hernandez, S. Baldelli and J. Bao, *Nat. Nanotechnol.*, 2014, **9**, 69–73.
41 Y. Zhao, B. Sun, X. Huang, H. Liu, D. Su, K. Sun and G. Wang, *J. Mater. Chem. A*, 2015, **3**, 5402–5408.
42 S. Lin, C. S. Diercks, Y. B. Zhang, N. Kornienko, E. M. Nichols, Y. Zhao, A. R. Paris, D. Kim, P. Yang, O. M. Yaghi and C. J. Chang, *Science*, 2015, **349**, 1208–1213.
43 H. He, P. Zapol and L. A. Curtiss, *J. Phys. Chem. C*, 2010, **114**, 21474–21481.
44 M. J. Kenney, M. Gong, Y. Li, J. Z. Wu, J. Feng, M. Lanza and H. Dai, *Science*, 2013, **342**, 836–840.
45 L. Chen, J. Yang, S. Klaus, L. J. Lee, R. Woods-Robinson, J. Ma, Y. Lum, J. K. Cooper, F. M. Toma, L. W. Wang, I. D. Sharp, A. T. Bell and J. W. Ager, *J. Am. Chem. Soc.*, 2015, **137**, 9595–9603.
46 J. Qiu, G. Zeng, M.-A. Ha, B. Hou, M. Mecklenburg, H. Shi, A. N. Alexandrova and S. B. Cronin, *Chem. Mater.*, 2015, **27**, 7977–7981.
47 S. Hu, M. R. Shaner, J. A. Beardslee, M. Lichterman, B. S. Brunschwig and N. S. Lewis, *Science*, 2014, **344**, 1005–1009.
48 M. Pourbaix, *Atlas of Electrochemical Equilibria in Aqueous Solutions*, Pergamon Press, New York, 1966.

